



Nanoscale

Coupling nanobubbles in 2D lateral heterostructures

Journal:	<i>Nanoscale</i>
Manuscript ID	NR-ART-01-2022-000512.R2
Article Type:	Paper
Date Submitted by the Author:	23-Apr-2022
Complete List of Authors:	Ambardar, Sharad; University of South Florida, Department of Physics Kamh, Rana; University of South Florida, Department of Electrical Engineering Withers, Zachary; University of South Florida, Department of Physics Sahoo, prasana; University of Cambridge, Cambridge Graphene Center Voronine, Dmitri ; University of South Florida, Department of Physics

SCHOLARONE™
Manuscripts

Coupling nanobubbles in 2D lateral heterostructures

Sharad Ambardar^a, Rana Kamh^b, Zachary H. Withers^c, Prasana K. Sahoo^d, and Dmitri V. Voronine^{a,c,*}

^a*Department of Medical Engineering, University of South Florida, Tampa, FL 33620*

^b*Department of Electrical Engineering, University of South Florida, Tampa, FL 33620*

^c*Department of Physics, University of South Florida, Tampa, FL 33620*

^d*Materials Science Centre, India Institute of Technology, Kharagpur, India*

Abstract

Two-dimensional transition metal dichalcogenides provide flexible platforms for nanophotonic engineering due to their exceptional mechanical and optoelectronic properties. For example, continuous band gap tunability has been achieved in 2D TMDs by elastic strain engineering. Localized elastic deformations in nanobubbles behave as “artificial atoms” with spatially varying band gap resulting in funnelling of excitons and photocarriers. Here we present a new method of nanobubble fabrication in monolayer 2D lateral heterostructures using high temperature superacid treatment. We fabricated MoS₂ and WS₂ nanobubbles and performed near-field imaging with nanoscale resolution using tip-enhanced photoluminescence (TEPL) spectroscopy. TEPL nanoimaging revealed the coupling between MoS₂ and WS₂ nanobubbles with a large synergistic PL enhancement due to plasmonic tip, hot electrons, and exciton funnelling. We investigated the contributions of different enhancement mechanisms, and developed a quantum plasmonic model, in good agreement with the experiments. Our work opens new avenues in exploration of novel nanophotonic coupling schemes.

Introduction

Two-dimensional (2D) transition metal dichalcogenides (TMDs) have recently emerged as promising materials for optoelectronic applications^{1,2}. Lateral and vertical heterostructures of 2D TMDs may be used to design new devices with controllable functionalities³⁻⁶. Micro and nano-sized bubbles in graphene revealed unique elastic and optical properties^{7,8}. Monolayer TMDs have been studied by strain engineering to control photoluminescence (PL)⁹⁻¹². Strain was correlated with bubble topography^{12,13}. Additionally, nanobubbles, nanotents and other nanostructures have been fabricated, having unique properties of quantum emitters¹⁴⁻¹⁷. These materials have enabled new explorations of fundamental physics at the nanoscale.

Heterogenous properties of 2D materials affect their nano-optical response. For example, superacid treatment by bis(trifluoromethane) sulfonimide (TFSI) was previously used to enhance the PL of MoS₂^{18,19}. However, previous work on characterization of micro/nano-sized bubbles was focused on single materials, without the comparison of the properties of bubbles in different TMDs under similar conditions, such as lateral heterostructures. Strain was used to create localized areas of high PL intensity, so-called “artificial atoms”, with tunable band gap via exciton funnelling^{12,20,21}. However, conventional far-field (FF) PL characterization techniques provide limited information about the nanoscale properties of nanobubbles. Therefore, we used high resolution near-field (NF) tip-enhanced PL (TEPL) imaging to improve the nanobubble characterization. Previously, NF PL imaging was used for characterizing excitons in MoS₂²²⁻²⁵ and WS₂²⁶⁻²⁸, 2D nanobubbles¹³, local strain control in WSe₂²⁹, probing dark excitons³⁰, and studying the nanoscale heterogenous³¹⁻³³ and quantum plasmonic effects³⁴ in 2D heterostructures. TEPL is based on the predominantly out-of-plane excitation by the electric field component polarized along the tip axis, perpendicular to the sample plane, which is less efficient than the in-plane excitation of 2D materials. TEPL signals can be enhanced by out-of-plane protrusions such as bubbles and wrinkles^{35,36}. Synergistic enhancement of MoS₂ PL by TFSI and gold nanoparticles has also been shown³⁷.

Here, we fabricated MoS₂ and WS₂ nanobubbles in monolayer 2D lateral heterostructure using high temperature TFSI treatment. We characterized nanobubbles using high-resolution TEPL imaging, which is not limited by diffraction, to obtain information about PL enhancement mechanisms and coupling. We observed large synergistic enhancement of PL signals, due to the coupled plasmonic antenna, hot electron, and exciton funnelling.

Experimental setup

Coupling nanobubbles in 2D materials is challenging due to their nanoscale size and limitations of the conventional fabrication and characterization techniques. Far-field PL imaging of exciton funneling was previously used to characterize TMD bubbles^{12,17}. Fig. 1A shows schematically that in isolated bubbles excitons are symmetrically attracted (dashed arrows) to the regions of smaller band gap in bubbles. However, the proximity of the two bubbles causes the band edge asymmetry (Fig. 1B), resulting in the directional funnelling from WS₂ bubble to MoS₂ bubble, coupling the bubbles (solid arrows in Fig. 1A). The photocarriers generated by excitons separated at the junction can transfer across the junction³⁸. The transfer distance can be increased

due to funneling to several hundred nm, which corresponds to the typical bubble width. Similar transfer of hot electrons across the junction was previously observed using TEPL in MoSe₂-WSe₂³⁴ and MoS₂-WS₂³⁹ heterostructures without bubbles. Therefore, the junction also has a direct effect on the funnelling and PL distribution in the vicinity of the bubbles, as shown here.

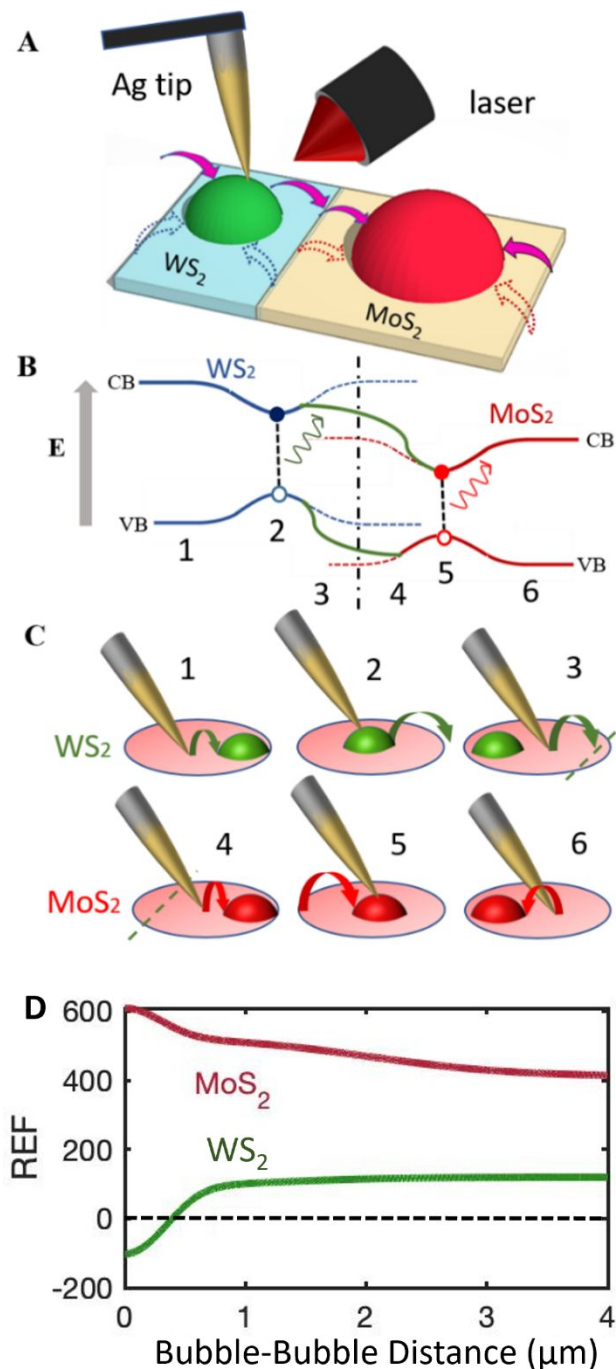


Figure 1. (A) Sketch of tip-enhanced photoluminescence (TEPL) experiment showing coupled MoS₂ and WS₂ nanobubbles (solid arrows). Funnelling is symmetric in the uncoupled bubbles (dotted arrows). (B) Schematic energy diagram for the symmetric uncoupled (dashed) and

directionally coupled (solid) WS₂ and MoS₂ nanobubbles. (C) Tip-sample-laser configurations showing laser excitation spot (red oval) with tip on flat (1,6), bubble (2,5), and junction (3,4) areas. (D) Theoretical relative enhancement factor (REF) as a function of bubble-to-bubble distance.

Conventional confocal PL imaging is limited in the spatial resolution of a few hundred nm. In contrast, TEPL has a spatial resolution of ~20 nm, and can be used to determine the PL enhancement and directional coupling of WS₂ and MoS₂ nanobubbles via a 2D lateral heterojunction.

Enhancement mechanisms

We identified four PL enhancement mechanisms: (i) bubble enhancement, which includes exciton funnelling; (ii) electromagnetic near-field tip enhancement; (iii) out-of-plane polarization tip enhancement on bubble; and (iv) synergistic enhancement due to the bubble-bubble coupling via exciton and hot electron funnelling.

Different mechanisms contribute to the PL enhancement when the tip is placed at different sample locations. Fig. 1C shows six tip-sample-laser configurations, which correspond to the locations 1-6 in Fig. 1B, when the tip is placed on the bubble (2,5), near the junction (3,4), or on flat areas near the bubble but far from the junction (1,6). Plasmonic Ag tip plays a role of a nanoantenna generating a larger number of excitons in a localized area (receiver) and enhancing the PL signal (emitter). Solid arrows in Fig. 1C illustrate the transport of excitons and photocarriers in coupled bubbles. Depending on tip location, excitons generated by the near and far fields transfer in and out of the tip-enhanced recombination area, leading to modified PL enhancement factors (EF). For example, when the tip is placed on the flat WS₂ (1) or MoS₂ areas (6) near the bubble, the tip-enhanced excitons transfer toward the bubble leading to a reduced EF. When the tip is placed on the coupled WS₂ (2) and MoS₂ bubbles (5), the photocarriers generated by separated funnelled excitons transfer across the junction, reducing PL of WS₂ and enhancing PL of MoS₂³⁴.

Figure 2 shows the graphical representation of six different EFs given by Eqs. (1) – (6) based on different combinations of the four enhancement mechanisms (i) – (iv), which are marked by the “x” symbols in Table 1 and are indicated by the following graphical symbols. *Large red circle* indicates the FF enhancement of the PL signal due to the funnelling mechanism (i) of the bubble. It is present in Figs. 2A, 2E and 2F and contributes to Eqs. (1), (5) and (6). *Blue shade on bubble* indicates the NF enhancement of the PL signal due to the funnelling mechanism (i) of the bubble. It is present in Figs. 2B, 2E and 2F and contributes to Eqs. (2), (5) and (6). *Blue shade on tip* indicates the NF enhancement of the PL signal due to the conventional TEPL mechanism (ii) on flat sample. It is present in Figs. 2C, 2D, 2E and 2F and contributes to Eqs. (3), (4), (5) and (6). *Small yellow circle* indicates the enhancement of the PL signal due to the out-of-plane tip-bubble mechanism (iii). It is present in Figs. 2B, 2D, 2E and 2F and contributes to Eqs. (2), (4), (5) and (6). *Red arrow* indicates the synergistic PL signal enhancement (or quenching) due to the bubble coupling mechanism (iv). It is present in Fig. 2F and contributes to Eqn. (6).

We obtained the following EF equations based on different combinations of the experimentally measured FF and NF PL signals on bubble (B) and flat (F) areas. *Eq. (1)*, shown in Fig. 2A,

describes the enhancement factor EF_{Out}^{BF} obtained by the ratio of FF PL signals on bubble (I_{FF}^B) and flat (I_{FF}^F) areas. This describes the FF bubble funnelling mechanism (i). If there is no funnelling, then the PL signals on both areas are the same, and the ratio of I_{FF}^B and I_{FF}^F equals 1, leading to $EF_{Out}^{BF} = 0$. Fig. 2A shows the graphical representation of this EF by the *large red circle* indicating the FF funnelling mechanism (i).

Eq. (2), shown in Fig. 2B, is the NF analog of Eq. (1). It describes the enhancement factor EF_{In}^{BF} , obtained by the ratio of NF PL on bubble (I_{NF}^B) and flat (I_{NF}^F) areas. This describes the mixed contribution of the NF bubble funnelling mechanism (i) and the out-of-plane polarization bubble-tip enhancement mechanism (iii). If there is no PL enhancement on the bubble, then the PL signals on both areas are the same, and the ratio of I_{NF}^B and I_{NF}^F equals 1, leading to $EF_{In}^{BF} = 0$. Fig. 2B shows the graphical representation of this EF by the *blue shade on bubble* indicating the NF enhancement due to the funnelling mechanism (i) and by the *small yellow circle* indicating the enhancement due to the out-of-plane tip-bubble mechanism (iii).

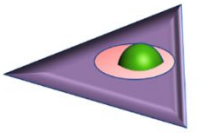
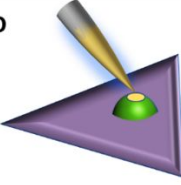
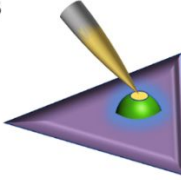
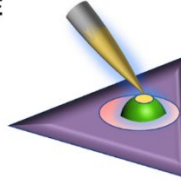
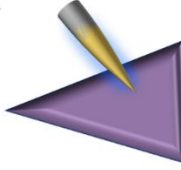
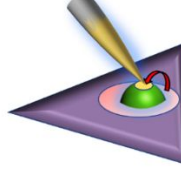
<p>A</p>  <p>Eq. 1</p> <p>FF Funnel</p> $\frac{I_{FF}^B}{I_{FF}^F} - 1$	<p>D</p>  <p>Eq. 4</p> <p>Tip on Bubble</p> $\frac{I_{NF}^B}{I_{FF}^F} \times \frac{S_{FF}}{S_{NF}}$
<p>B</p>  <p>Eq. 2</p> <p>NF Funnel</p> $\frac{I_{NF}^B}{I_{NF}^F} - 1$	<p>E</p>  <p>Eq. 5</p> <p>Tip and Funnel</p> $\frac{I_{NF}^B - I_{NF}^F}{I_{FF}^F} \times \frac{S_{FF}}{S_{NF}} + \left(\frac{I_{FF}^B}{I_{FF}^F} - 1 \right)$
<p>C</p>  <p>Eq. 3</p> <p>Tip on Flat</p> $\frac{I_{NF}^F}{I_{FF}^F} \times \frac{S_{FF}}{S_{NF}}$	<p>F</p>  <p>Eq. 6</p> <p>Synergistic Coupling</p> $\frac{I_{NF}^B}{I_{FF}^F} \times \frac{S_{FF}}{S_{NF}} + \left(\frac{I_{FF}^B}{I_{FF}^F} - 1 \right)$

Figure 2. Graphical representation of the PL enhancement factors for coupled WS₂ and MoS₂ nanobubbles.

Eq. (3), shown in Fig. 2C, is the conventional TEPL equation due to mechanism (ii) used to calculate the EF from the comparison of the measured PL intensities on the flat area with tip ($I_{Tip In}^F$) and on the flat area without tip ($I_{Tip Out}^F$) with the multiplication by the surface area scaling factor ($\frac{S_{FF}}{S_{NF}}$):

$$EF_{In}^F = \left(\frac{I_{Tip In}^F}{I_{Tip Out}^F} - 1 \right) \times \frac{S_{FF}}{S_{NF}} = \frac{I_{NF}^F}{I_{FF}^F} \times \frac{S_{FF}}{S_{NF}}$$

where $I_{Tip\ Out}^F = I_{FF}^F$ corresponds to the measured FF PL signal with the tip out of contact with the sample, and $I_{Tip\ In}^F = I_{NF}^F + I_{FF}^F$ corresponds to the measured PL signal when the tip is in contact with the sample. The scaling factor $(\frac{S_{FF}}{S_{NF}})$ is used to make sure that the same number of molecules is used for the comparison of the NF and FF signals. If there is no near field enhancement on the flat area, then $I_{NF}^F = 0$ and there is no TEPL, leading to $EF_{In}^F = 0$. Fig. 2C shows the graphical representation of this EF by the *blue shade on tip* indicating the near-field enhancement of the PL signal due to the conventional TEPL mechanism (ii).

Eq. (4), shown in Fig. 2D, is the bubble analog of Equation (3). The enhancement factor EF_{In}^B has contributions of both the in-plane (ii) and out-of-plane (iii) mechanisms, and is obtained by the tip-in and tip-out measurements on the bubble area analogous to those on flat area described in Equation (3):

$$EF_{In}^B = \left(\frac{I_{Tip\ In}^B}{I_{Tip\ Out}^B} - 1 \right) \times \frac{S_{FF}}{S_{NF}} = \frac{I_{NF}^B}{I_{FF}^B} \times \frac{S_{FF}}{S_{NF}}.$$

If there is no near field enhancement on the bubble area, then $I_{NF}^B = 0$ and there is no TEPL on the bubble, leading to $EF_{In}^B = 0$. Fig. 2D shows the graphical representation of this EF by the *blue shade on tip* indicating the near-field in-plane TEPL mechanism (ii) and by the *small yellow circle* indicating the enhancement due to the out-of-plane tip-bubble mechanism (iii).

Eq. (5) is obtained after expansion of the following equation shown in Fig. 2E, which describes the non-synergistic enhancement factor EF_{NS} , which includes the three mechanisms (i)-(iii) as the sum of the product of the NF enhancement factors $EF_{In}^{BF} \times EF_{In}^F$ and the FF enhancement factor EF_{Out}^{BF} :

$$EF_{NS} = \left(\frac{I_{NF}^B}{I_{NF}^F} - 1 \right) \times \frac{I_{NF}^F}{I_{FF}^F} \times \frac{S_{FF}}{S_{NF}} + \left(\frac{I_{FF}^B}{I_{FF}^F} - 1 \right).$$

Fig. 2E shows the graphical representation of this EF by the *large red circle* and *blue shade on bubble* due to the funnelling mechanism (i), *blue shade on tip* indicating the near-field in-plane TEPL mechanism (ii) and by the *small yellow circle* indicating the enhancement due to the out-of-plane tip-bubble mechanism (iii).

Finally, Eq. (6), shown in Fig. 2E, describes the total enhancement factor EF_{Tot} , obtained from the comparison of the FF PL intensities on the bubble (I_{FF}^B) and on the flat area (I_{FF}^F), and the corresponding NF PL signals (I_{NF}^B and I_{NF}^F) multiplied by the surface area scaling factor $(\frac{S_{FF}}{S_{NF}})$, which gives Eq. (6). It includes all four mechanisms (i)-(iv). Fig. 2F shows the graphical representation of this EF by the *large red circle* and *blue shade on bubble* due to the funnelling mechanism (i), *blue shade on tip* indicating the near-field in-plane TEPL mechanism (ii), the *small yellow circle* indicating the enhancement due to the out-of-plane tip-bubble mechanism (iii) and by the *red arrow* indicating the synergistic enhancement (or quenching) due to the bubble coupling mechanism (iv).

Results

Figure S1A shows the AFM height image of the TFSI-treated monolayer MoS₂-WS₂ heterostructure, which reveals multiple randomly distributed nanobubbles. Due to the atomic thickness and smooth contrast between the two materials, the heterojunction was not clearly visible. First, we selected two isolated, uncoupled WS₂ and MoS₂ nanobubbles in the vicinity of the junction, separated by $\sim 2 \mu\text{m}$, and indicated by red crosses in Fig. S1A. The geometric properties of the two nanobubbles are shown in the zoomed-in AFM height image in Fig. S1B and in the AFM height profile in Fig. S1C. We label these bubbles as W1 and Mo1, respectively.

The PL measurements with 633 nm excitation allowed for the mapping of the full spectral band of MoS₂ centred at 675 nm and a part of the spectral band of WS₂ at 635 nm as shown in the FF PL spectra of WS₂ (Fig. S1F) and MoS₂ (Fig. S1G). The chosen locations correspond to the regions of interest 2-5 in Fig. 1C. Significant PL enhancement on the bubble as compared to the flat area was observed in both materials. The corresponding enhancement factors $\mathbf{EF}_{\text{Out}}^{\text{BF}}$ are shown using Eq. (1) in Table 1. The EFs were calculated based on the FF and NF PL intensities (I_{FF}^{F} , I_{FF}^{B} , I_{NF}^{F} , and I_{NF}^{B}) measured on the bubble (B) and flat (F) areas, respectively. Note that the flat areas were chosen on the side of the bubble away from the junction, to avoid alloying effects (see discussion below). The FF PL on MoS₂ was enhanced by $\sim 4\%$ and on WS₂ by $\sim 30\%$ due to the exciton funnelling mechanism. The larger funnelling efficiency in WS₂ could be due to its larger dipole moment compared to MoS₂. To further enhance the PL signals and to obtain the nanoscale resolution, we coupled the laser to the plasmonic Au-coated Ag tip as shown in Fig. 1A. The TEPL spectra in Figs. S1D and S1E show a significant enhancement of the NF PL signals on bubbles as compared to the flat areas.

Near-field PL imaging also gives an opportunity to investigate the spatially heterogenous optical properties of 2D materials. Fig. 3 shows the NF PL maps of the *uncoupled* WS₂ (W1) and MoS₂ (Mo1) nanobubbles obtained by integrating the PL signals in the selected spectral ranges highlighted in red and green shaded areas in Figs. S1D and S1E. The AFM topographic image (Fig. 3B) is correlated with the TEPL maps (Figs. 3A and 3C), revealing a high degree of PL localization in the vicinity of the bubbles. Note that the smaller particles on the left side of the WS₂ nanobubbles are not the bubbles but the random particles from oxidation products of CVD growth or ambient oxidation that do not show any PL enhancement. We performed FF Raman and TERS measurements using 532 nm laser excitation to confirm the presence of the 2D materials and nanobubbles or random particles. The random particles did not show any NF Raman signal enhancement (Fig. S6).

The experimental EF profiles in Figs. 3D and 3E were calculated using Eqs. (3) and (4) for the flat and bubble areas, respectively. As explained in the Enhancement mechanisms section with Fig. 2, these EFs reflect contributions of the (ii) and (iii) mechanisms that use tip as antenna enhancing NF PL signals without the synergistic contribution of hot electron transfer across the junction. The latter is shown as total enhancement factor, \mathbf{EF}_{Tot} , in Table 1. The corresponding raw intensity data are shown in supplementary Fig. S7.

Next we compared these experimental EF profiles with theoretically calculated EFs, shown in Figs. 3F and 3G. The details of the theoretical model are given in Supplementary materials and are discussed below. Overall, both the experiments and theory showed good agreement, with positive EF values in the bubble areas. This corresponds to the symmetric funnelling shown by dashed lines in Fig. 1A. The small asymmetry observed in these profiles is due to the symmetry breaking effect of the junction. It does not lead to negative EF values, indicative of the coupling, as shown below.

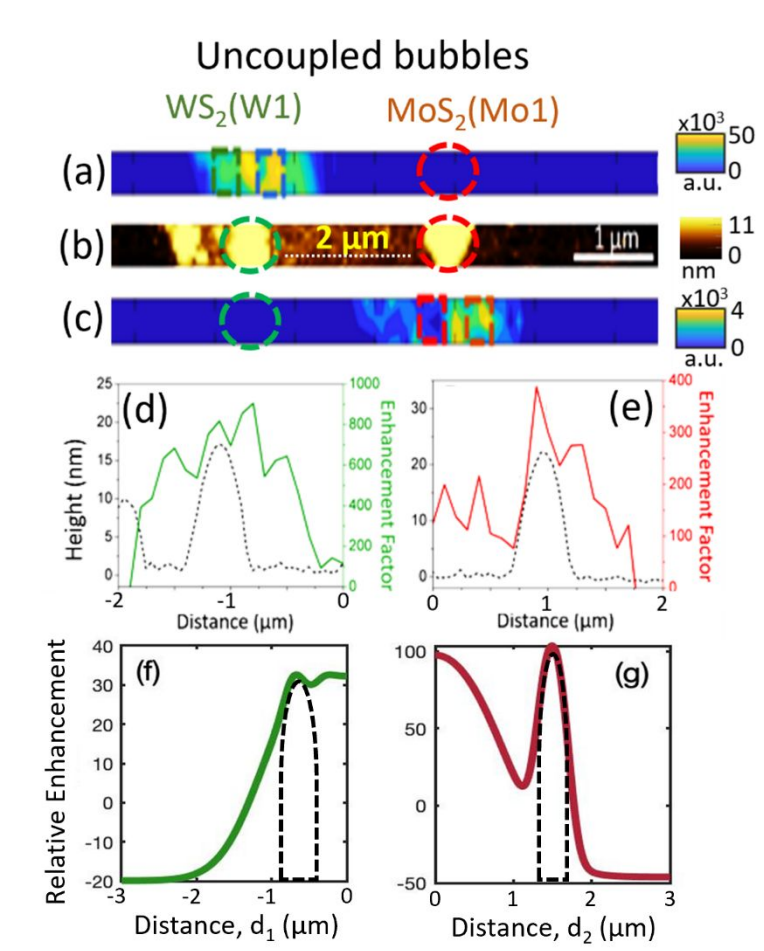


Figure 3. Near-field imaging of *uncoupled* nanobubbles: WS₂ (A) and MoS₂ (C) TEPL images are correlated with the AFM height image (B) of a monolayer lateral MoS₂-WS₂ heterostructure on a SiO₂/Si substrate. The white dotted line in (B) indicates the 2 μm distance between the MoS₂ and WS₂ bubbles. Dashed circles indicate the positions of bubbles. Dashed rectangular areas highlight the asymmetry between the sides of the bubbles closer and further from a junction. Experimental PL enhancement factors (EF) for the WS₂ (D) and MoS₂ (E) bubbles are shown overlapped with AFM height profiles (dotted lines). Theoretical PL EFs for the WS₂ (F) and MoS₂ (G) bubbles are shown overlapped with height profiles (dashed lines).

To investigate coupling, we performed near-field PL imaging of another pair of the *coupled* WS₂ (W2) and MoS₂ (Mo2) nanobubbles separated by a smaller distance (~ 760 nm) across the junction (Fig. 4). The AFM topographic image (Fig. 4B) is correlated with the TEPL maps (Figs. 4A and 4C), revealing a high degree of PL localization in the vicinity of the Mo2 bubble. However, the

PL and AFM signals are not well overlapped in the case of the W2 bubble. In fact, the TEPL signal has a negative dip, as shown in the EF profile in Fig. 4E. This characteristic negative EF dip is a direct feature of the bubble coupling as described by the theoretical model below and is confirmed in the theoretical EF in Fig. 4G. In contrast, both the experimental (Fig. 4D) and theoretical (Fig. 4F) EF profiles of Mo₂ bubble have positive values and do not show the negative signal on the bubble. This confirms the good agreement between the theoretical model and experiments. Note that the particle at the junction (in AFM image in Fig. 4B near the dashed white line) is not the bubble but the random particle from oxidation products of CVD growth or ambient oxidation that do not show any PL enhancement.

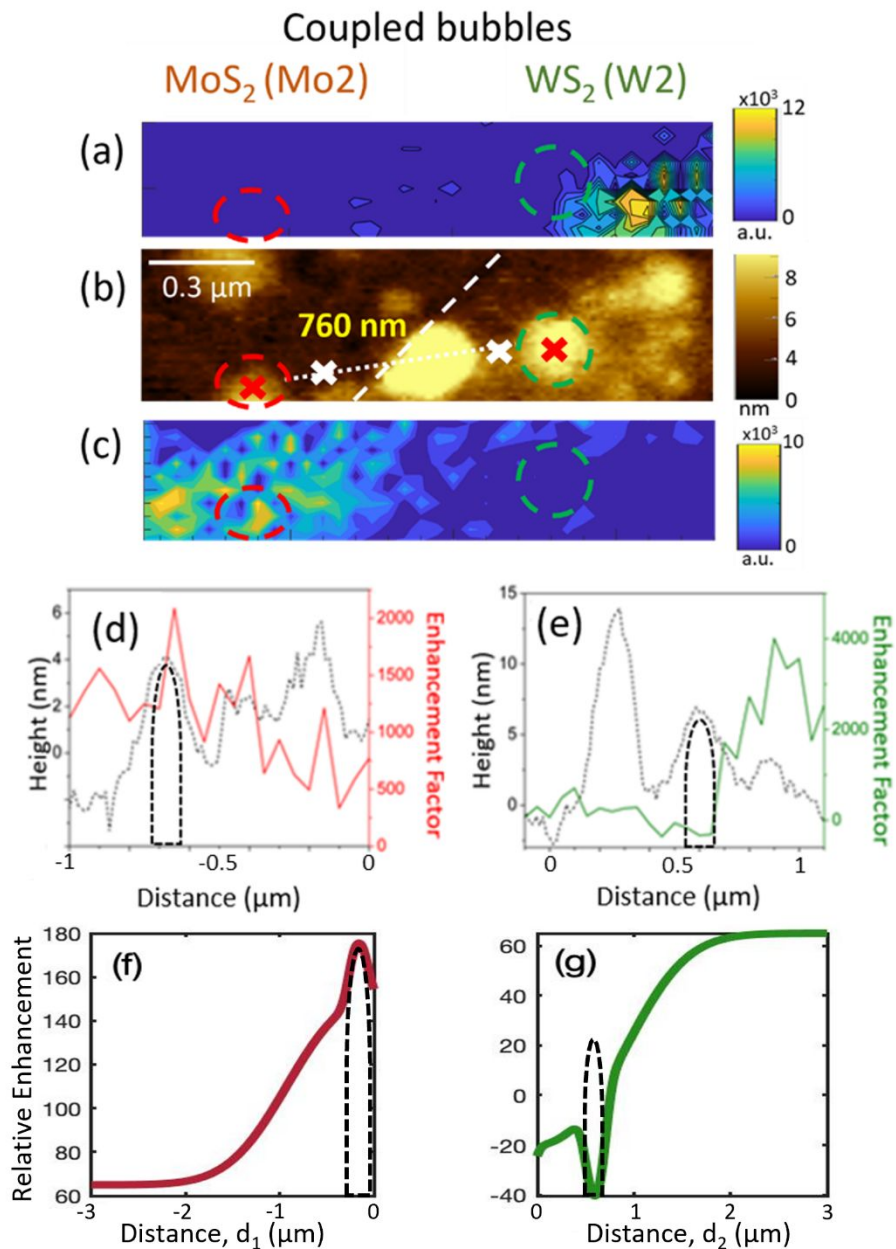


Figure 4. Near-field imaging of *coupled* nanobubbles: WS₂ (A) and MoS₂ (C) TEPL images are correlated with the AFM height image (B) of a monolayer lateral MoS₂-WS₂ heterostructure on a SiO₂/Si substrate. The white dotted line in (B) indicates the 760 nm distance between the MoS₂ and WS₂ bubbles. White dashed line shows the junction. Dashed circles indicate the positions of bubbles. Experimental PL enhancement factors (EF) for the MoS₂ (D) and WS₂ (E) bubbles are shown overlapped with AFM height profiles (dotted lines). Theoretical PL EFs for the MoS₂ (F) and WS₂ (G) bubbles are shown overlapped with height profiles (dashed lines).

To distinguish between the bubbles and particles, we performed Kelvin probe force microscopy (KPFM) measurements (Fig. 5). We measured both the capacitance gradient and contact potential difference (CPD) signals, which both showed significant differences and were able to clearly distinguish between the particles and bubbles. The nature of the capacitance difference is the different chemical composition of the particles and bubbles. The capacitance gradient correlates well with the CPD signals under optical excitation. The basis for the CPD sensitivity is the different response of bubbles and particles to light. We measured CPD with (Figs. 5b and 5f) and without (Figs. 5d and 5h) laser excitation. Bubbles are sensitive to resonant optical excitation, generating excitons and free carriers which significantly modify the CPD signal. However, the particles are not resonant and, therefore, are insensitive to the light. The corresponding CPD signals from the particles are not significantly modified and form dips in the CPD profiles, which are distinguishable from the bubbles, which do not form dips. Other small particles at the edge of the flake show similar dips (indicated by a blue arrow in Fig. 5).

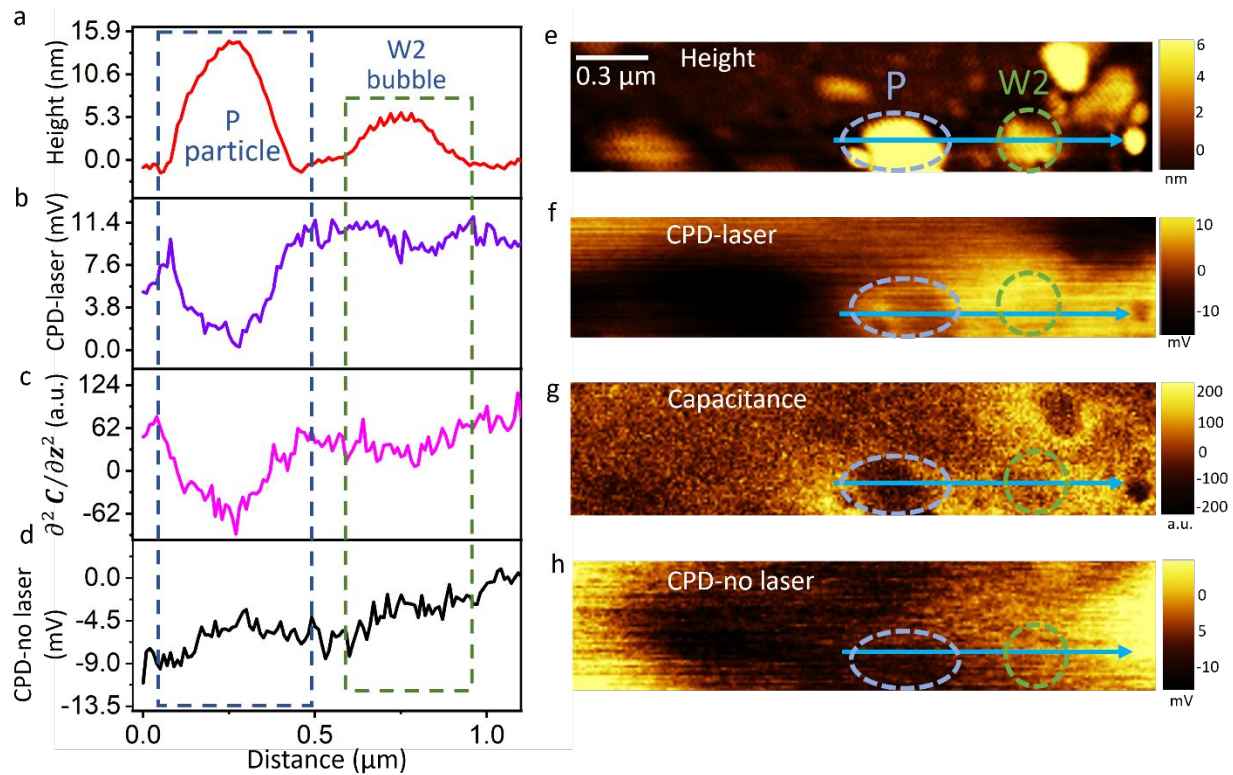


Figure 5. Kelvin probe force microscopy (KPFM) of bubbles and particles. (a) AFM height profile that corresponds to the blue arrow line in height map (e). (b) Contact potential difference (CPD) profile that corresponds to the line in CPD map (f), both of which were obtained with ~ 0.1 mW illumination with 532 nm laser. (c) Capacitance gradient profile that corresponds to the capacitance gradient map (g). (d) CPD profile that corresponds to the line in CPD map (h), both of which were obtained without laser illumination. Blue ellipse and green circle highlight the particle and WS_2 (W2) bubble, respectively.

The EF values for the uncoupled (W1 and Mo1) and coupled (W2 and Mo2) nanobubbles are presented in Table 1.

<i>Enhancement Factor</i>	<i>Mechanism</i>				<i>WS₂ (W1)</i>	<i>MoS₂ (Mo1)</i>	<i>WS₂ (W2)</i>	<i>MoS₂ (Mo2)</i>
	(i)	(ii)	(iii)	(iv)				
$\text{EF}_{\text{Out}}^{\text{BF}}$	x				0.3	0.04	0.17	-0.25
$\text{EF}_{\text{In}}^{\text{BF}}$	x		x		0.7	1.5	-1.11	-0.26
$\text{EF}_{\text{In}}^{\text{F}}$		x			559	118	3138	1540
$\text{EF}_{\text{In}}^{\text{B}}$		x	x		726	284	-273	1520
EF_{NS}	x	x	x		382	176	-3457	-404
EF_{Tot}	x	x	x	x	941	294	-319	1136

Table 1. Enhancement factors (EF) for the MoS_2 and WS_2 parts of the monolayer lateral heterostructure on bubble (B) and flat (F) areas with (In) and without (Out) plasmonic tip. The EF values were calculated using Eqs. (1) - (6) described above for the uncoupled (W1 and Mo1) and coupled (W2 and Mo2) nanobubbles.

We developed a theoretical model to describe the tip-sample distance dependence of the uncoupled pure MoS_2 and WS_2 materials as well as the coupled MoS_2 and WS_2 nanobubbles based on the combination of our previous models of MoSe_2 - WSe_2 ³⁴ and MoS_2 - WS_2 ³⁹ heterostructures without nanobubbles (see Supplementary Materials). Briefly, the PL signals of MoS_2 and WS_2 are proportional to the populations of exciton states $|X\rangle$ and $|Y\rangle$, respectively, which are coupled to the ground state $|g\rangle$, and the corresponding higher states $|X^0\rangle$ and $|Y^0\rangle$. TEPL enhancement factors were simulated by solving Eqs. (S5) - (S11) in steady state as relative enhancements ΔN of MoS_2 (N_X) and WS_2 (N_Y) populations equal to the differences between the corresponding near-field (NF) and far-field (FF) signals at 0.36 nm and 20 nm tip-sample distance, respectively: $\Delta N_X = N_X(0.36\text{nm}) - N_X(20\text{nm})$ and $\Delta N_Y = N_Y(0.36\text{nm}) - N_Y(20\text{nm})$.

We used this model to simulate the relative enhancement factor (REF) defined as $(\frac{I_{tip In}^B}{I_{tip Out}^B} - 1)PF$ at the center of each bubble as a function of bubble-to-bubble distance (Fig. 1D). The Purcell factor (PF) of 2×10^3 was used based on the previously found values for 2D materials³⁰. We assumed a symmetric case where the bubbles are equidistant from the junction on the opposite sides. We used the FWHM of the bubble height of 350 nm based on average experimental values. Fig. 1D shows the enhancement of MoS₂ and quenching of WS₂ signals in the proximity of the junction. The coupling distance of approximately twice the FWHM of the bubble height is observed, where WS₂ shows negative REF values. The experimental bubble-bubble distances of ~ 760 nm and $2 \mu\text{m}$ for the coupled (Fig. 4) and uncoupled (Fig. 3) bubbles are in agreement with the theoretical prediction.

Discussion

The enhancement of the FF PL signals without the tip due to the mechanism (i) is described by $\mathbf{EF}_{\text{Out}}^{\text{BF}}$ represents spatially averaged information over the bubble area due to the limited FF spatial resolution. The NF analogue of Eq. (1) is given by Eq. (2) for the enhancement factor $\mathbf{EF}_{\text{In}}^{\text{BF}}$, which provides an improved description of funnelling with a higher spatial resolution. It shows larger $\mathbf{EF}_{\text{In}}^{\text{BF}}$ values compared to $\mathbf{EF}_{\text{Out}}^{\text{BF}}$ for both uncoupled bubbles W1 and Mo1 (Table 1). Also, as expected, the $\mathbf{EF}_{\text{In}}^{\text{BF}}$ value of the coupled W2 bubble is smaller compared to $\mathbf{EF}_{\text{Out}}^{\text{BF}}$ value because of the more pronounced negative quenching signal, which gets averaged out in the far-field case of $\mathbf{EF}_{\text{Out}}^{\text{BF}}$. Also, $\mathbf{EF}_{\text{In}}^{\text{BF}}$ of W2 bubble is smaller than -1, because of the negative I_{NF}^{B} signal of WS₂ bubble due to the coupling to MoS₂ bubble. However, both mechanisms (i) and (iii) contribute to $\mathbf{EF}_{\text{In}}^{\text{BF}}$. Therefore, further analysis of other EFs is needed to separate these contributions. Note that the small negative values of the $\mathbf{EF}_{\text{Out}}^{\text{BF}}$ and $\mathbf{EF}_{\text{In}}^{\text{BF}}$ of Mo2 bubble are due to the possible allying effect and the uneven distribution of MoS₂ material close to the junction. These values may be ignored and the positive value of the total enhancement factor for Mo2 bubble still support the coupling mechanism, as shown below.

To understand the effects of other mechanisms, we investigate the EFs given by Eqs. (3)-(6). For example, the values of $\mathbf{EF}_{\text{In}}^{\text{F}}$ and $\mathbf{EF}_{\text{In}}^{\text{B}}$ in Eqs. (3) and (4), respectively, correspond to the tip enhancement on flat and bubble areas. $\mathbf{EF}_{\text{In}}^{\text{F}}$ is the conventional TEPL enhancement factor determined by the in-plane tip enhancement mechanisms (ii). $\mathbf{EF}_{\text{In}}^{\text{B}}$ is the analogous TEPL enhancement factor on the bubble and is determined by both the in-plane (ii) and out-of-plane (iii) mechanisms. The out-of-plane mechanism (iii) is due to the PL enhancement of the non-flat part of the 2D material (bubble) by the polarization component of the near-field along the tip axis^{29,36}. These EFs are normalized by the areas for the near-field (S_{NF}) and far-field (S_{FF}) excitation spots, where $S_{\text{FF}} = \pi R_{\text{FF}}^2$ with the FF excitation spot radius $R_{\text{FF}}=500$ nm and $S_{\text{NF}} = \pi R_{\text{NF}}^2$ with NF spot size equal to the tip apex radius $R_{\text{NF}}=10$ nm. Surprisingly, the value of $\mathbf{EF}_{\text{In}}^{\text{F}}$ on WS₂ is larger than on MoS₂ for both the flat areas near the uncoupled and coupled bubbles (Table 1), which could be explained due to the stronger light-matter coupling and slight p-doping nature of WS₂. However, the value of $\mathbf{EF}_{\text{In}}^{\text{B}}$ on WS₂ is negative for the coupled W2 bubble and is positive for the uncoupled W1 bubble, indicating the PL intensity quenching due to the coupling to the MoS₂ bubble as

expected based on the schematic in Fig. 1A and the theoretical model. These EFs are influenced by the mechanisms (ii) and (iii), in which the tip is used as an antenna probing the bubble coupling by funnelling. Here the tip is used as a nanoscale reporter and does not contribute to the coupling.

The combination of the three mechanisms (i)-(iii), where tip only performs the passive role of a reporter is presented in the non-synergistic \mathbf{EF}_{NS} shown in Table 1. It shows the coupling of nanobubbles via the junction without the active influence by the tip. However, the tip may also contribute to the bubble coupling effect, for example, via hot electron injection into the WS_2 flat area and subsequent hot electron transfer to WS_2 bubble and then to MoS_2 bubble. This additional flat-bubble-tip-bubble coupling effect may be observed as synergistic contribution to the total enhancement factor, \mathbf{EF}_{Tot} , which includes an additional synergistic mechanism (iv), as shown in Eq. (6) in Table 1. It is schematically represented by the four solid arrows in Fig. 1A. The subtraction of I_{NF}^{F} in the numerator in Eq. (5), compared Eq. (6), explains the synergistic effect in \mathbf{EF}_{Tot} , since subtracting I_{NF}^{F} from the numerator eliminates the “near-field flat-to-bubble” coupling effects. As a result, the final \mathbf{EF}_{Tot} of the coupled WS_2 bubble is still negative, and both the uncoupled WS_2 and MoS_2 , as well as the coupled MoS_2 bubbles all have positive values. All four mechanisms are included in the combined synergistic \mathbf{EF}_{Tot} , which provides direct evidence of coupling with and without the contributions of the plasmonic tip. Thus, our discovered additional tip-induced bubble coupling mechanism could be used in developing new active nanophotonic devices.

To simplify the near-field analysis we also calculated the contrast factors (CF) for the uncoupled bubbles W1 and Mo1 shown in Figure 3, and for the coupled bubbles W2 and Mo2 in Figure 4 (Table S1). The difference in the CF values of the coupled bubbles is larger than the uncoupled as shown in Table S1 and shows a lower value of the W2 bubble ($\text{CF} < -1$), which indicates quenching of the NF PL signal due to coupling.

Materials and Methods

Monolayer lateral MoS_2 - WS_2 heterostructures were grown on a SiO_2/Si substrate in a quartz tube using a one-pot chemical vapor deposition (CVD) system as previously described⁶. The CVD growth resulted in the formation of a smooth junction (white dashed line in Fig. S1A) between MoS_2 and WS_2 . Similar smooth junctions with ~ 230 nm width were previously characterized using TEPL imaging of monolayer lateral MoSe_2 - WSe_2 heterostructures³³. The nanobubbles in CVD-grown monolayer lateral MoS_2 - WS_2 heterostructures were generated by following the previously reported TFSI superacid treatment procedure¹⁹ that was modified by increasing the temperature. Briefly, TFSI (20 mg) was dissolved in 1,2-dichloromethane and 1,2-dichlorobenzene to produce a 0.2 mg/ml solution, in which the heterostructures on SiO_2/Si substrates were submerged for 10 minutes at 150°C and then removed and dried with nitrogen.

AFM imaging, FF PL imaging, NF TEPL, Raman, TERS and KPFM imaging were performed using a confocal optical microscope (LABRam, Horiba) coupled to a scanning probe microscope (OmegaScopeR, Horiba) with 633 nm or 532 nm laser focused using objective lens ($\text{NA} = 0.9$) on the Au-coated Ag tip with the tip apex radius of ~ 10 nm. The radius of the laser focal spot was ~ 500 nm. The FF PL and NF TEPL measurements were performed with ~ 20 nm and ~ 0.36 nm tip-sample distance, respectively. AFM and FF PL measurements were performed in the tapping

mode with the 20 nm average tip-sample distance. NF TEPL imaging was performed in the contact mode. We separated the NF and FF signals by subtracting the Tip-out (TSD of 20 nm) maps from the Tip-in (TSD of 0.36 nm) maps. The subtracted maps are pure NF maps and do not contain any FF contribution. Using backscattering configuration with a 632.57 nm edge filter, the scattered signal was collected and detected by spectrometer with 600 g/mm grating coupled to a CCD camera. FF PL and NF TEPL maps were obtained using acquisition time of 0.2 s and 0.5 mW laser power. The detailed setup for the TEPL experiments was previously described⁴⁰. The PL signal was collected by the illumination objective. The angle between the incident laser optical axis and the horizontal sample plane was 25°. The angle between the tip and the sample plane was 78°. The incident light polarization was along the tip axis. The tip and the laser were stationary during the experiments, while the sample stage was scanned.

We used 633 nm laser excitation for TEPL because this wavelength better matches the plasmon resonance of the tip and provides largest near field enhancement. On the other hand, we used 532 nm laser excitation for basic material characterization using Raman spectroscopy and TERS, because the Raman and PL signals are separated for this excitation wavelength. However, for 633 nm excitation they overlap, and the Raman signals are overwhelmed by the strong PL. TERS experiments with 532 nm laser excitation were performed using the same microscope setup as for the 633 nm laser excitation described above. Both tip-in and tip-out spectra were obtained with 0.1 mW laser power and 1 s acquisition time. Using backscattering configuration with a 532.13 nm edge filter, the scattered signal was collected and detected using a spectrometer with 1800 g/mm grating coupled to a CCD camera. The far-field Raman map was obtained using 532 nm excitation with 1 mW laser power and 5 s acquisition time. The KPFM measurements with 532 nm excitation were performed under the same conditions as in the TERS measurements described above.

The tapping mode FF PL signal may contain a possible contribution of the NF PL. However, under our experimental conditions with low incident power, short acquisition time and the specific plasmonic tip properties and tip-laser-sample configuration, the NF PL contributions are negligible. This has been confirmed in the control TERS experiments on carbon nanotubes (CNT) performed under identical conditions as shown in Figure S4. No CNT image was clearly identified in the FF signal in Fig. S4b. Also, the tip-out (20 nm) Raman spectrum in Fig. S4c shows no signal from CNT.

The effect of the shaft of the tip in the FF PL measurements at 20 nm average tip-sample distance is negligible, because our investigated bubble height is smaller than 20 nm and bubble width is larger than 300 nm. With such aspect ratio of more than 10 and tip curvature radius of ~ 10 nm, we expect the negligible interaction with the tip shaft. TEPL intensity could be expected to be higher on the borders compared to the middle part of the bubbles due to the strain-induced funneling mechanism (i) and the out-of-plane polarization mechanism (iii). However, this effect was not resolved in the experiment, possibly due to the large aspect ratio.

We performed the laser power dependence of FF PL and NF TEPL maps of the MoS₂-WS₂ lateral heterostructure with for low (0.1 mW) and high (1 mW) incident laser power, respectively. The results showed that PL and Raman spectra did not vary significantly under the different laser powers and, therefore, the low laser power illumination used in the presented experiments did not affect the sample. Supplementary Figure S9 shows the absence of damage effects using Raman and PL spectra of MoS₂-WS₂ heterostructure before and after high power measurements. The

spectra did not show any significant differences such as broadening, new peaks or changes in peak ratios.

Monolayer thickness of 2D lateral heterostructures was confirmed by AFM measurements (Fig. S8).^{41,42} AFM height profile showed average monolayer thickness of < 1 nm (Fig. S8B).

We performed additional experiments on two more pairs of uncoupled and coupled nanobubbles, which showed similar results, consistent with those presented in Figs. 2 and 3.

Conclusions

In summary, we have studied the coupling of MoS₂ and WS₂ nanobubbles by the plasmonic antenna tip and a heterojunction using tip-enhanced near-field imaging. The observed quenching of the PL signals provides experimental and theoretical evidence for the coupling. The work provides a step towards developing new coupled quantum emitters based on 2D nanobubbles are promising candidates for quantum information and communication applications.

Author Contributions

D.V.V conceived the idea and designed the experiments., P.K.S. prepared the sample. D.V.V., S.A. and P.K.S. performed the experiments. D.V.V., S.A., R.K., Z.H.W. and P.K.S. analyzed the results. D.V.V., S.A., R.K., Z.H.W. and P.K.S. wrote the paper.

Conflicts of interest

There are no conflicts to declare.

Acknowledgements

We thank Andrey Krayev and Max Wetherington for helpful discussions. D.V.V. acknowledges the support by the National Science Foundation (Grant No. CHE-1609608).

References

- 1 K. F. Mak, C. Lee, J. Hone, J. Shan and T. F. Heinz, *Physical review letters*, 2010, **105**, 136805.
- 2 A. Splendiani, L. Sun, Y. Zhang, T. Li, J. Kim, C.-Y. Chim, G. Galli and F. Wang, *Nano letters*, 2010, **10**, 1271–1275.
- 3 A. K. Geim and I. V. Grigorieva, *Nature*, 2013, **499**, 419–425.
- 4 J. R. Schaibley, H. Yu, G. Clark, P. Rivera, J. S. Ross, K. L. Seyler, W. Yao and X. Xu, *Nature Reviews Materials*, 2016, **1**, 1–15.
- 5 Z. Zhang, P. Chen, X. Duan, K. Zang, J. Luo and X. Duan, *Science*, 2017, **357**, 788–792.
- 6 P. K. Sahoo, S. Memaran, Y. Xin, L. Balicas and H. R. Gutiérrez, *Nature*, 2018, **553**, 63–67.

- 7 J. Zabel, R. R. Nair, A. Ott, T. Georgiou, A. K. Geim, K. S. Novoselov and C. Casiraghi, *Nano letters*, 2012, **12**, 617–621.
- 8 E. Khestanova, F. Guinea, L. Fumagalli, A. K. Geim and I. V. Grigorieva, *Nature communications*, 2016, **7**, 1–10.
- 9 S. Bertolazzi, J. Brivio and A. Kis, *ACS nano*, 2011, **5**, 9703–9709.
- 10 P. Johari and V. B. Shenoy, *ACS nano*, 2012, **6**, 5449–5456.
- 11 H. J. Conley, B. Wang, J. I. Ziegler, R. F. Haglund Jr, S. T. Pantelides and K. I. Bolotin, *Nano letters*, 2013, **13**, 3626–3630.
- 12 A. V. Tyurnina, D. A. Bandurin, E. Khestanova, V. G. Kravets, M. Koperski, F. Guinea, A. N. Grigorenko, A. K. Geim and I. V. Grigorieva, *ACS Photonics*, 2019, **6**, 516–524.
- 13 T. P. Darlington, C. Carmesin, M. Florian, E. Yanev, O. Ajayi, J. Ardelean, D. A. Rhodes, A. Ghiotto, A. Krayev and K. Watanabe, *Nature Nanotechnology*, 2020, 1–7.
- 14 N. Levy, S. A. Burke, K. L. Meaker, M. Panlasigui, A. Zettl, F. Guinea, A. C. Neto and M. F. Crommie, *Science*, 2010, **329**, 544–547.
- 15 N. N. Klimov, S. Jung, S. Zhu, T. Li, C. A. Wright, S. D. Solares, D. B. Newell, N. B. Zhitenev and J. A. Stroscio, *Science*, 2012, **336**, 1557–1561.
- 16 C. Palacios-Berraquero, D. M. Kara, A. R.-P. Montblanch, M. Barbone, P. Latawiec, D. Yoon, A. K. Ott, M. Loncar, A. C. Ferrari and M. Atatüre, *Nature communications*, 2017, **8**, 1–6.
- 17 G. D. Shepard, O. A. Ajayi, X. Li, X. Y. Zhu, J. Hone and S. Strauf, *2D Materials*, 2017, **4**, 021019.
- 18 M. Amani, D.-H. Lien, D. Kiriya, J. Bullock and A. Javey, *Near-unity photoluminescence quantum yield in MoS₂*, Google Patents, 2017.
- 19 M. Amani, P. Taheri, R. Addou, G. H. Ahn, D. Kiriya, D.-H. Lien, J. W. Ager III, R. M. Wallace and A. Javey, *Nano letters*, 2016, **16**, 2786–2791.
- 20 J. Feng, X. Qian, C.-W. Huang and J. Li, *Nature Photonics*, 2012, **6**, 866.
- 21 H. Li, A. W. Contryman, X. Qian, S. M. Ardakani, Y. Gong, X. Wang, J. M. Weisse, C. H. Lee, J. Zhao and P. M. Ajayan, *Nature communications*, 2015, **6**, 1–7.
- 22 W. Bao, N. J. Borys, C. Ko, J. Suh, W. Fan, A. Thron, Y. Zhang, A. Buyanin, J. Zhang and S. Cabrini, *Nature communications*, 2015, **6**, 1–7.
- 23 Y. Lee, S. Park, H. Kim, G. H. Han, Y. H. Lee and J. Kim, *Nanoscale*, 2015, **7**, 11909–11914.
- 24 W. Su, N. Kumar, S. Mignuzzi, J. Crain and D. Roy, *Nanoscale*, 2016, **8**, 10564–10569.
- 25 Y. Okuno, O. Lancry, A. Tempez, C. Cairone, M. Bosi, F. Fabbri and M. Chaigneau, *Nanoscale*, 2018, **10**, 14055–14059.

- 26 C. Kastl, C. T. Chen, T. Kuykendall, B. Shevitski, T. P. Darlington, N. J. Borys, A. Krayev, P. J. Schuck, S. Aloni and A. M. Schwartzberg, *2D Materials*, 2017, **4**, 021024.
- 27 Y. Lee, S. J. Yun, Y. Kim, M. S. Kim, G. H. Han, A. K. Sood and J. Kim, *Nanoscale*, 2017, **9**, 2272–2278.
- 28 Z. He, Z. Han, J. Yuan, A. M. Sinyukov, H. Eleuch, C. Niu, Z. Zhang, J. Lou, J. Hu and D. V. Voronine, *Science advances*, 2019, **5**, eaau8763.
- 29 K.-D. Park, O. Khatib, V. Kravtsov, G. Clark, X. Xu and M. B. Raschke, *Nano letters*, 2016, **16**, 2621–2627.
- 30 K.-D. Park, T. Jiang, G. Clark, X. Xu and M. B. Raschke, *Nature nanotechnology*, 2018, **13**, 59–64.
- 31 W. Xue, P. K. Sahoo, J. Liu, H. Zong, X. Lai, S. Ambardar and D. V. Voronine, *Journal of Vacuum Science & Technology A: Vacuum, Surfaces, and Films*, 2018, **36**, 05G502.
- 32 Y. Kim, S. J. Yun, E. Lee and J. Kim, *Optical Materials Express*, 2019, **9**, 1864–1871.
- 33 P. K. Sahoo, H. Zong, J. Liu, W. Xue, X. Lai, H. R. Gutiérrez and D. V. Voronine, *Optical Materials Express*, 2019, **9**, 1620–1631.
- 34 C. Tang, Z. He, W. Chen, S. Jia, J. Lou and D. V. Voronine, *Physical Review B*, 2018, **98**, 041402.
- 35 A. Castellanos-Gomez, R. Roldán, E. Cappelluti, M. Buscema, F. Guinea, H. S. van der Zant and G. A. Steele, *Nano letters*, 2013, **13**, 5361–5366.
- 36 A. Bhattarai, A. Krayev, A. Temiryazev, D. Evplov, K. T. Crampton, W. P. Hess and P. Z. El-Khoury, *Nano Letters*, 2018, **18**, 4029–4033.
- 37 Y. Zeng, W. Chen, B. Tang, J. Liao, J. Lou and Q. Chen, *RSC advances*, 2018, **8**, 23591–23598.
- 38 M. Z. Bellus, M. Mahjouri-Samani, S. D. Lane, A. D. Oyedele, X. Li, A. A. Puretzky, D. Geoghegan, K. Xiao and H. Zhao, *ACS nano*, 2018, **12**, 7086–7092.
- 39 Z. H. Withers, S. Ambardar, X. Lai, J. Liu, A. Zhukova and D. V. Voronine, *arXiv preprint arXiv:2001.10138*.
- 40 Y. Zhang, D. V. Voronine, S. Qiu, A. M. Sinyukov, M. Hamilton, Z. Liege, A. V. Sokolov, Z. Zhang and M. O. Scully, *Scientific reports*, 2016, **6**, 1–9.
- 41 H. Li, Q. Zhang, C.C.R. Yap, B.K. Tay, T.H.T. Edwin, A. Oliver, D. Baillargeat, *Advanced Functional Materials*, 2012, **22**, 1385–1390.
- 42 A. Berkdemir, H.R. Gutierrez, A.R. Botello-Mendez, N. Perea-Lopez, A.L. Elias, C.-I. Chia, B. Wang, V.H. Crespi, F. Lopez-Urias and J.-C. Charlier, *Scientific reports*, 2013, **3**, 1–8.